

Title	The structural conversion from $\alpha$ -AgVO <sub>3</sub> to $\beta$ -AgVO <sub>3</sub> : Ag nanoparticle decorated nanowires with application as cathode materials for Li-ion batteries
Authors	McNulty, David; Ramasse, Quentin; O'Dwyer, Colm
Publication date	2016-08-19
Original Citation	McNulty, D., Ramasse, Q. and O'Dwyer, C. (2016) 'The structural conversion from $\alpha$ -AgVO <sub>3</sub> to $\beta$ -AgVO <sub>3</sub> : Ag nanoparticle decorated nanowires with application as cathode materials for Li-ion batteries,' <i>Nanoscale</i> , 8, pp. 16266-16275. doi: 10.1039/C6NR04825K
Type of publication	Article (peer-reviewed)
Link to publisher's version	10.1039/c6nr04825k
Rights	© The Royal Society of Chemistry 2016
Download date	2024-04-25 06:34:16
Item downloaded from	<a href="https://hdl.handle.net/10468/3167">https://hdl.handle.net/10468/3167</a>

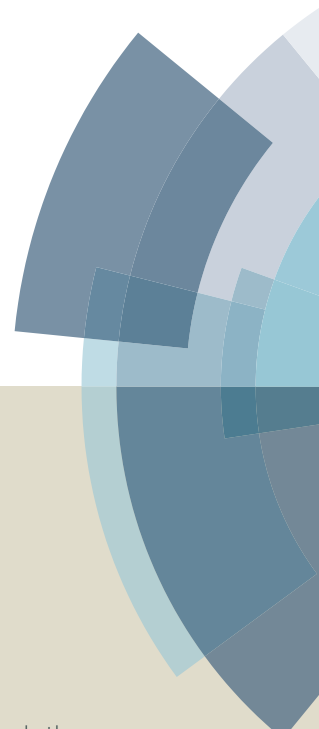


**UCC**

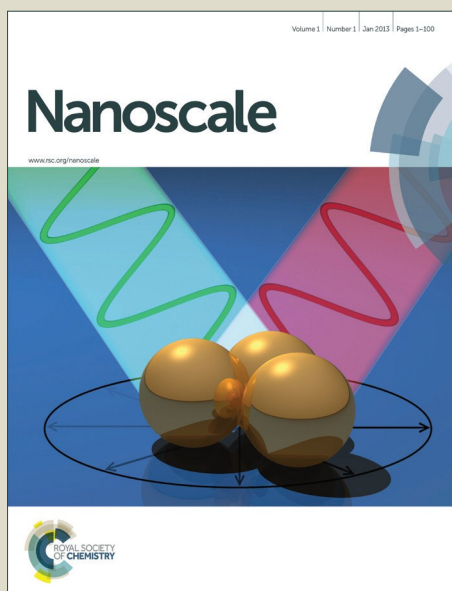
**University College Cork, Ireland**  
Coláiste na hOllscoile Corcaigh

# Nanoscale

Accepted Manuscript



This article can be cited before page numbers have been issued, to do this please use: D. McNulty, Q. Ramasse and C. O'Dwyer, *Nanoscale*, 2016, DOI: 10.1039/C6NR04825K.



This is an *Accepted Manuscript*, which has been through the Royal Society of Chemistry peer review process and has been accepted for publication.

*Accepted Manuscripts* are published online shortly after acceptance, before technical editing, formatting and proof reading. Using this free service, authors can make their results available to the community, in citable form, before we publish the edited article. We will replace this *Accepted Manuscript* with the edited and formatted *Advance Article* as soon as it is available.

You can find more information about *Accepted Manuscripts* in the [Information for Authors](#).

Please note that technical editing may introduce minor changes to the text and/or graphics, which may alter content. The journal's standard [Terms & Conditions](#) and the [Ethical guidelines](#) still apply. In no event shall the Royal Society of Chemistry be held responsible for any errors or omissions in this *Accepted Manuscript* or any consequences arising from the use of any information it contains.

## The Structural Conversion from $\alpha$ -AgVO<sub>3</sub> to $\beta$ -AgVO<sub>3</sub>: Ag Nanoparticle Decorated Nanowires with Application as Cathode Materials for Li-ion Batteries

Received 00th January 20xx,  
Accepted 00th January 20xx

DOI: 10.1039/x0xx00000x

www.rsc.org/

David McNulty,<sup>a</sup> Quentin Ramasse,<sup>b</sup> and Colm O'Dwyer<sup>a,c\*</sup>

The majority of electrode materials in batteries and related electrochemical energy storage devices are fashioned into slurries via the addition of a conductive additive and a binder. However, aggregation of smaller diameter nanoparticles in current generation electrode compositions can result in non-homogeneous active materials. Inconsistent slurry formulation may lead to inconsistent electrical conductivity throughout the material, local variations in electrochemical response, and the overall cell performance. Here we demonstrate the hydrothermal preparation of Ag nanoparticle (NP) decorated  $\alpha$ -AgVO<sub>3</sub> nanowires (NWs) and their conversion to the tunnel structured  $\beta$ -AgVO<sub>3</sub> NWs by annealing to form a uniform blend of intercalation materials that are well connected electrically. The synthesis of nanostructures with chemically bound conductive nanoparticles is an elegant means to overcome the intrinsic issues associated with electrode slurry production, as these wire-to-wire conductive pathways are formed within the overall electrode active mass of NWs. The conversion from  $\alpha$ -AgVO<sub>3</sub> to  $\beta$ -AgVO<sub>3</sub> is explained in detail through a comprehensive structural characterization. Meticulous EELS analysis of  $\beta$ -AgVO<sub>3</sub> NWs offers insight into the true  $\beta$ -AgVO<sub>3</sub> structure and how the annealing process facilitates a higher surface coverage of Ag NPs directly from ionic Ag content within the  $\alpha$ -AgVO<sub>3</sub> NWs. Variations in vanadium oxidation state across the surface of the nanowires indicate that the  $\beta$ -AgVO<sub>3</sub> NWs have a core-shell oxidation state structure, and that the vanadium oxidation state under the Ag NP confirms a chemically bound NP from reduction of diffused ionic silver from the  $\alpha$ -AgVO<sub>3</sub> NWs core material. Electrochemical comparison of  $\alpha$ -AgVO<sub>3</sub> and  $\beta$ -AgVO<sub>3</sub> NWs confirms that  $\beta$ -AgVO<sub>3</sub> offers improved electrochemical performance. An *ex-situ* structural characterization of  $\beta$ -AgVO<sub>3</sub> NWs after the first galvanostatic discharge and charge offers new insight into the Li<sup>+</sup> reaction mechanism for  $\beta$ -AgVO<sub>3</sub>. Ag<sup>+</sup> between the van der Waals layers of the vanadium oxide is reduced during discharge and deposited as metallic Ag, the vacant sites are then occupied by Li<sup>+</sup>.

### Introduction

Silver vanadium oxides (SVOs) have attracted a tremendous amount of attention due to their high gravimetric/volumetric energy densities and high power.<sup>1-6</sup> Many of the pioneering reports on the electrochemical performance of SVO as a cathode material have been reported by E. S. Takeuchi et al.<sup>7-10</sup> The most well-known application of SVO is the use of Ag<sub>2</sub>V<sub>4</sub>O<sub>11</sub> as a cathode material in lithium batteries for advanced biomedical devices such as the implantable cardiac defibrillator.<sup>1</sup> Previous reports have suggested

that the higher Ag:V molar ratio of  $\beta$ -AgVO<sub>3</sub> compared to Ag<sub>2</sub>V<sub>4</sub>O<sub>11</sub> serves to improve electrochemical performance.<sup>11, 12</sup> There have been several recent reports on the synthesis of  $\beta$ -AgVO<sub>3</sub> nanostructures for use in lithium ion batteries; Zeng et al. reported on the preparation of  $\beta$ -AgVO<sub>3</sub> nanoribbons via a water evaporation method<sup>13</sup>, Wu et al. prepared  $\beta$ -Ag<sub>0.33</sub>V<sub>2</sub>O<sub>5</sub> nanostructures via an electrospinning technique followed by a hydrothermal process<sup>14</sup> and Han et al. utilised a substrate-assisted hydrothermal method to synthesize moundlike radial  $\beta$ -AgVO<sub>3</sub> nanowire clusters.<sup>15</sup> As a result of its structural and electrochemical properties,  $\beta$ -AgVO<sub>3</sub> has also been investigated for use in many other applications, such as for use in electrochromic devices, as an antimicrobial agent, in photocatalysis and for use in sensors.<sup>16-21</sup> Active materials decorated with Ag NPs have shown superior performance in terms of increased conductivity, catalytic activity and sensing properties.<sup>22-24</sup> Recent reports have suggested that the presence of metallic silver in the active material may result in a significant increase in the conductivity of SVOs<sup>16, 25</sup>, which in electrochemical

<sup>a</sup> Department of Chemistry, University College Cork, Cork, T12 YN60, Ireland.

<sup>b</sup> SuperSTEM Laboratory, SciTech Daresbury Campus, Daresbury WA4 4AD, UK

<sup>c</sup> Micro-Nano Systems Centre, Tyndall National Institute, Lee Maltings, Cork, T12 RSCP, Ireland.

\* E-mail: c.odwyer@ucc.ie; Fax: +353 (0)21 4274097; Tel: +353 (0)21 4902732

Electronic Supplementary Information (ESI) available: Additional information on the  $\alpha$ -AgVO<sub>3</sub> and  $\beta$ -AgVO<sub>3</sub> NWs structure and electrochemistry, and supplementary figures. See DOI: 10.1039/x0xx00000x

technologies such as batteries, facilitate improved electrochemical performance in terms of specific capacity as well as capacity retention.

For commercial applications it is essential to develop simple, fast and low cost synthesis methods for electrode materials. Herein we report on the facile, high yield synthesis of  $\alpha$ -AgVO<sub>3</sub> and  $\beta$ -AgVO<sub>3</sub> nanowires (NWs) decorated with Ag nanoparticles (NPs). Many commonly used cathode materials such as LiNi<sub>1/3</sub>Mn<sub>1/3</sub>Co<sub>1/3</sub>O<sub>2</sub>, possess low electronic conductivity.<sup>26</sup> The widespread approach to overcome this issue is to composite the active material with conductive carbon-based additives to enhance the electrical conductivity of the cathode material.<sup>27, 28</sup> However a recent report has shown that, for low mass loadings, an interconnected conductive network could not be constructed from carbon blacks due to a tendency for the small diameter carbon particles to aggregate.<sup>29</sup> The use of non-homogeneous slurries is a potentially serious issue that is often overlooked in the literature and can lead to incorrectly calculated specific capacity values. Recent reports suggest that carbon nanotubes, which can act as conductive bridges, may be a more suitable conductive additive rather than traditionally used carbon blacks.<sup>30, 31</sup> Ag NPs have also been investigated as a means of increasing electrical conductivity and have shown to improve the electrochemical performance of materials such as TiO<sub>2</sub> and Li<sub>4</sub>Ti<sub>5</sub>O<sub>12</sub>.<sup>32, 33</sup> The  $\alpha$ -AgVO<sub>3</sub> and  $\beta$ -AgVO<sub>3</sub> NWs we present herein are both decorated with Ag NPs. There is a higher density of Ag NPs on the surface of the  $\beta$ -AgVO<sub>3</sub> NW, which we analyse in detail, that also facilitates electrical bridging between inter-wire contacts to enhance the nanowire network conductivity in the absence of any binders. Synthesising electrode materials that are decorated with conductive nanoparticles is an elegant means of overcoming the need to mechanically mix conductive particles with the electrode material under investigation. The Ag NPs are chemically bound to the  $\alpha$ -AgVO<sub>3</sub> and  $\beta$ -AgVO<sub>3</sub> NWs, which also removes the necessity to add a binder.

This report details the preparation of  $\alpha$ -AgVO<sub>3</sub> NWs via a hydrothermal treatment and the structural conversion from  $\alpha$ -AgVO<sub>3</sub> to the tunnel-structured  $\beta$ -AgVO<sub>3</sub> by annealing at 475 °C. We initially compare  $\alpha$ -AgVO<sub>3</sub> and  $\beta$ -AgVO<sub>3</sub> NWs structurally prior to electrochemical testing. Electron energy loss spectroscopy (EELS) of  $\beta$ -AgVO<sub>3</sub> NWs demonstrates that the oxidation state of vanadium varies across the surface of the NW, moving from the interface between an Ag NP and a NW to the surface of the core of a NW. It has previously been suggested that the electrochemical performance of  $\beta$ -AgVO<sub>3</sub> is superior to  $\alpha$ -AgVO<sub>3</sub> due to a particular tunnel structure that accommodates cations.<sup>13, 34</sup> In this report we systemically investigate and compare the electrochemical performance of  $\alpha$ -AgVO<sub>3</sub> and  $\beta$ -AgVO<sub>3</sub> NWs via cyclic voltammetry and galvanostatic testing. The electrochemical response demonstrates that interactions with Li<sup>+</sup> are more reversible for  $\beta$ -AgVO<sub>3</sub> NWs and that higher specific capacity values can be obtained. The higher density of Ag NPs on the surface of the heated NWs as well as the structural conversion to the more stable  $\beta$ -AgVO<sub>3</sub> phase is directly correlated to an improvement in electrochemical performance. In order to offer insight into the Li<sup>+</sup> reaction mechanism with the conversion to Ag-NP decorated  $\beta$ -AgVO<sub>3</sub> NWs, we uncovered the specific response to lithiation after

the first discharge and charge. TEM and XPS analysis verifies that Ag<sup>+</sup> present in the van der Waals gaps of the crystallographic structure of vanadate are reduced to Ag<sup>0</sup> and deposited as metallic silver.

## Experimental Section

### Synthesis of $\alpha$ -AgVO<sub>3</sub> and $\beta$ -AgVO<sub>3</sub> NWs

Silver vanadium oxide NWs were prepared via hydrothermal treatment of a mixture of ammonium metavanadate and silver nitrate, using a modified version of a previously reported method.<sup>16</sup> Typically, 0.3 g of NH<sub>4</sub>VO<sub>3</sub> and 0.5 of Synperonic F 108 (C<sub>3</sub>H<sub>6</sub>O.C<sub>2</sub>H<sub>4</sub>O)<sub>x</sub> were added together and then dissolved in solution of nitric acid in deionised water (15:1 v/v solution of DI water and 1 M HNO<sub>3</sub>). The mixture was stirred at 500 rpm for 3 hours at room temperature and then 1.1 g of AgNO<sub>3</sub> was added. The mixture was then stirred for 1 additional hour before being transferred to a Teflon lined stainless steel autoclave. The mixture was then heated at 120 °C for 24 hours. The resulting yellow powder was rinsed with DI water and then dried using a Buchner funnel.

### Material Characterization

Thermogravimetric analysis (TGA) was performed using a Mettler Toledo TGA/DSC1. AgVO<sub>x</sub> NW samples were placed in an alumina crucible and heated to 475°C at a heating rate of 5°C min<sup>-1</sup> and then cooled, in a nitrogen atmosphere. Conventional TEM analysis was conducted using a JEOL JEM-2100 TEM operating at 200 kV. Further analysis was then carried out using a dedicated Nion UltraSTEM 100MC scanning transmission electron microscope (STEM). The instrument was operated at 60 kV acceleration voltage to minimize any potential beam-induced damage to the wire surface and their interface with Ag nanoparticles. The optics of the microscope were configured to for a 33 mrad beam convergence semi-angle, corresponding to an estimated probe size of approximately 0.9 Å. High-angle annular-dark-field (HAADF) images were recorded using a detector with inner and outer semi-angles of 88 mrad and 190 mrad, respectively. The native beam energy width of 0.32 eV of the instrument was further reduced through the use of a beam monochromator, resulting in an energy resolution (estimated from the zero loss peak full-width at half-maximum when observed in vacuum) of 0.15 eV. This allowed the observation of finer details in the V L<sub>2,3</sub> electron energy loss (EEL) edge fine structure, using the Gatan Enfinium ERS EEL spectrometer with which the microscope is equipped. The collection semi-angle for the EELS data was 44 mrad. EELS spectrum images were acquired by rastering the beam across a defined area of the sample, and recording serially an EEL spectrum at each point. Chemical maps can then be generated by integrating the signal intensity over a suitable energy window (20 eV for the Ag M<sub>4,5</sub> and V L<sub>2,3</sub> in this case) above the relevant ionization edge after subtraction of the decaying background using a power law model. Principal component analysis was carried out on spectrum images to reduce noise prior to generating chemical maps; however, no such

processing was applied for fine structure analysis to prevent any possible artifact induced by the mathematical treatment.

SEM analysis was performed using an FEI Quanta 650 FEG high resolution SEM at an accelerating voltage of 10 kV. Raman scattering spectroscopy was performed using an Ocean Optics QE65PRO Raman Spectrometer with a Laser Quantum GEM DPSS single transverse mode CW laser emitting at  $\lambda = 532$  nm and spectra were collected using a CCD camera. The beam was focused onto the samples using a 40 $\times$  objective lens. XRD analysis was performed using a Phillips Xpert PW3719 diffractometer using Cu K $\alpha$  radiation. (Cu K $\alpha$ ,  $\lambda = 0.15418$  nm, operation voltage 40 kV, current 40 mA). X-ray photoelectron spectroscopy was performed using a Kratos Axis 165 equipped with a monochromatic Al source (K $\alpha = 1486.58$  eV) with a spot size of 1 mm. The source power was 150 W, the take-off angle was set normal to the sample surface, the construction and peak fittings in the narrow region spectra were performed using a Shirley type background. Adventitious carbon was used for the charge reference (C 1s) for each measurement.

### Electrochemical Characterization

All electrochemical results presented in this report were performed using a BioLogic VSP Potentiostat/Galvanostat. The electrolyte consisted of a 1 mol dm $^{-3}$  solution of lithium hexafluorophosphate salts in a 1:1 (v/v) mixture of ethylene carbonate in dimethyl carbonate + 3 wt% vinylene carbonate. The electrochemical properties of AgVO $_x$  NWs were investigated in a half cell configuration against a pure Li counter electrode in a two electrode, stainless steel split cell (a coin cell assembly that can be disassembled for post-mortem analysis). No additional conductive additives or binders were added. Cyclic voltammetry was performed using a scan rate of 0.1 mV s $^{-1}$  in a potential window of 3.5 – 1.5 V. Galvanostatic testing was performed using a series of different specific currents ranging from 25 mA/g – 100 mA/g in a potential window of 3.5 – 1.5 V.

### Results and Discussion

The as prepared  $\alpha$ -AgVO $_3$  NWs were heated to 475  $^{\circ}$ C in N $_2$ , in order to ensure phase pure  $\beta$ -AgVO $_3$  NW formation and a high density of Ag NP surface decoration with a well-defined interface between the Ag NPs and the NW surface. SEM and TEM characterization in Figure 1a,c and Figure S1 of  $\alpha$ -AgVO $_3$  NWs demonstrates that they typically have lengths of 100 – 200  $\mu$ m and diameters of 100 – 150 nm. The as-synthesized AgVO $_x$  NWs are decorated with Ag NPs, which remain present after heating as shown in the TEM images in Figure 1b,d. Ag NPs are formed on the NW surface by reduction of AgNO $_3$ , which is in excess so as to provide a Ag source for AgVO $_3$  formation and surface-decoration by Ag via Ag $^+$  to Ag $^0$  reduction.<sup>17, 35</sup> Thermal ripening of the reduced Ag $^+$  on the surface of HT-grown  $\alpha$ -AgVO $_3$  (*vide infra*) forms a higher density coverage of Ag NPs on the  $\beta$ -AgVO $_3$  NW surface. Also, many of the NPs on the surface of the  $\beta$ -AgVO $_3$  NWs are quite small, with diameters on the order of  $\sim$ 5 nm. The additional NPs are possibly formed by a reduction of AgVO $_3$  during annealing and the structural conversion from  $\alpha$ -AgVO $_3$  to  $\beta$ -AgVO $_3$ . The electron diffraction pattern in Figure 1e was indexed to

the  $\alpha$ -AgVO $_3$  phase. Upon heating to 475  $^{\circ}$ C in N $_2$ , the electron diffraction pattern of the NW (Figure 1f) confirms a phase transformation to the tunnel-structured  $\beta$ -AgVO $_3$ .

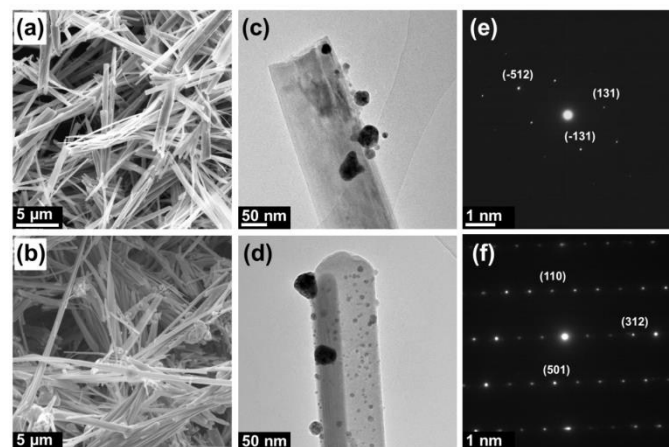


**Fig. 1.** SEM images (a) and (b), TEM images (c) and (d) and electron diffraction patterns (e) and (f) of AgVO $_x$  nanowires before and after heating to 475 $^{\circ}$ C in N $_2$ .

Thermogravimetric analysis of HT-grown  $\alpha$ -AgVO $_3$  NWs in Figure 2a, indicates that just 7% mass is lost when heated to 475  $^{\circ}$ C. This is in agreement with previous studies on silver vanadates.<sup>16, 36</sup> The derivative thermogravimetric curve shown in Figure 2a consists of 2 main peaks at 191  $^{\circ}$ C and 257  $^{\circ}$ C, corresponding to mass losses of 1.6 and 4.0 % respectively. The initial mass losses up to  $\sim$  200  $^{\circ}$ C are most likely due to the removal of physisorbed and chemisorbed water. The mass loss in the temperature range from 220 – 300  $^{\circ}$ C is due to the loss of coordinated water within the vanadate.<sup>16</sup>

Figure 2b displays the Raman spectra for AgVO $_x$  NWs before and after heating to 475  $^{\circ}$ C in N $_2$ . Although the NWs look quite similar before and after heating, electron diffraction analysis confirms a definite reconstruction to  $\beta$ -AgVO $_3$  from  $\alpha$ -AgVO $_3$  while additional Ag forms on the NW surface. The Raman spectrum for the  $\beta$ -AgVO $_3$  NWs after heating is in close agreement with Raman spectra previously reported for  $\beta$ -AgVO $_3$ .<sup>37, 38</sup> The weak band at 956 cm $^{-1}$  is attributed to the symmetric stretching of VO $_4$ .<sup>39</sup> The strong band at 892 cm $^{-1}$  may be due to either bridging V-O-Ag or O-V-O vibrations.<sup>38</sup> After annealing, the reduction of Ag $^+$  to Ag $^0$  during crystallographic phase change to  $\beta$ -AgVO $_3$  enhances the intensity of the V-O-Ag mode. The bands at 849 and 812 cm $^{-1}$  can be assigned to the stretching vibrations of VO $_3$  groups in the (V $_2$ O $_7$ ) $^{4-}$  ion and the stretching vibrations of Ag-O-Ag bridges respectively.<sup>40, 41</sup> The band observed at 737 cm $^{-1}$  is present due to the bridging V-O-V bond.<sup>34</sup> The weak band at 330 cm $^{-1}$  can be assigned to the asymmetric deformation modes of VO $_4$ .<sup>42</sup> Many of the characteristic vibrational bands for AgVO $_3$  are also present before heating the  $\alpha$ -AgVO $_3$  NWs to 475  $^{\circ}$ C, namely the bands present at 892, 812 and 737 cm $^{-1}$  respectively. However, the highest intensity band for the as-synthesized NWs is the band present at 924 cm $^{-1}$ ; this band is not observed in the Raman spectrum for the NWs after heating and can be attributed to the asymmetric stretching of VO $_4$  units, which are no longer present due to the conversion to the  $\beta$ -AgVO $_3$  crystal with a tunnel structured arrangement with coordinated Ag.<sup>39</sup>

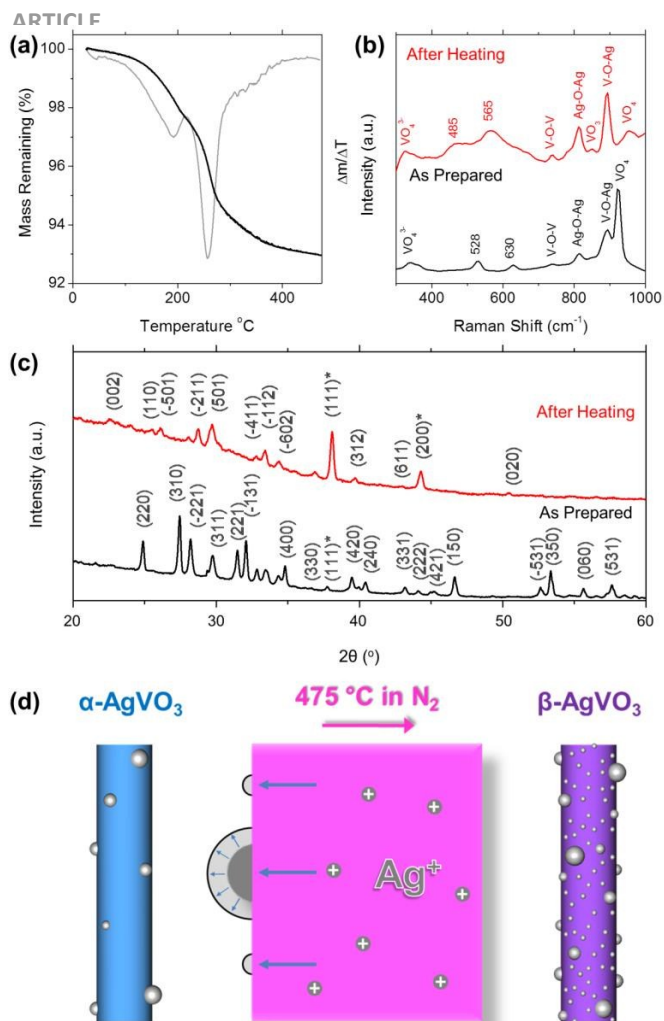


**Fig. 2.** (a) Thermogravimetric analysis and derivative mass loss curves for AgVO<sub>3</sub> nanowires heated to 475 °C in N<sub>2</sub> at a ramp rate of 5 °C/min (b) Raman spectra and (c) XRD patterns of AgVO<sub>3</sub> nanowires before and after heating to 475 °C in N<sub>2</sub>. Reflections labelled with \* correspond to cubic Ag. (d) Schematic representation of the transition from α-AgVO<sub>3</sub> to β-AgVO<sub>3</sub> upon heating to 475 °C in N<sub>2</sub>.

The XRD patterns for AgVO<sub>x</sub> NWs before and after heating to 475 °C in N<sub>2</sub> are shown in Figure 2c. The reflections observed in the XRD pattern for as-prepared NWs can be readily indexed to α-AgVO<sub>3</sub> phase with a *C2/c* space group (JCPDS 00-089-4396). Both XRD patterns also contain reflections (marked with \*) for cubic Ag metal with a *Fm-3m* space group (JCPDS 00-004-0783), due to the Ag NPs present on the surface of the NWs. Interestingly, the relative intensity of the reflections due to Ag metal content increases after annealing - the pure Ag metal content on the surface is formed from ionic silver from the α-AgVO<sub>3</sub> lattice and formed as a surface coverage of NPs after heating. In fact, the highest intensity peak for β-AgVO<sub>3</sub> NWs is the (111) for metallic Ag, indicating a high Ag content on the surface of the β-AgVO<sub>3</sub> NWs. The XRD pattern for the heated NWs contains reflections for only one phase of silver vanadium oxide, namely the β-AgVO<sub>3</sub> phase, a *Cm* space group (JCPDS 00-029-1154). This is in agreement with the Raman spectra presented in Figure 2b, whereby the spectrum for the heated NWs was a close match to previously reported spectra for β-AgVO<sub>3</sub>.<sup>34</sup> α-

AgVO<sub>3</sub> is known to be a metastable phase that when heated above 200 °C is converted into β-AgVO<sub>3</sub><sup>43</sup>; here we verify that when α-AgVO<sub>3</sub> is heated to higher temperatures (475 °C) the structural conversion occurs and the β-AgVO<sub>3</sub> structure is retained. A schematic representation of the transition from α-AgVO<sub>3</sub> to β-AgVO<sub>3</sub> is illustrated in Figure 2d. During heating to 475 °C in N<sub>2</sub>, Ag<sup>+</sup> ions within the nanowire structure are reduced to Ag metal, consequently the Ag NPs which were already on the surface of the α-AgVO<sub>3</sub> NWs can grow in size and additional smaller Ag NPs are formed on the surface of the NWs.

High resolution bright field (BF) and high-angle annular dark-field (HAADF) STEM images of β-AgVO<sub>3</sub> NWs are shown in Figure 3. Dark field imaging reveals a strong contrast ratio between the NWs and the NPs on the surface, as shown in Figure 3a and b, due to the large atomic number difference between the Ag NPs and the body of the NWs, the former therefore appearing much brighter in this imaging mode (which is often referred to as Z-contrast imaging). The HAADF image of the heated NWs reveals that the β-AgVO<sub>3</sub> NWs are comprehensively decorated with Ag NPs. Figure 3c,d show BF and HAADF images of Ag NPs on the surface of a β-AgVO<sub>3</sub> NWs. β-AgVO<sub>3</sub> NWs are decorated with a greater amount of smaller NPs than the HT prepared α-AgVO<sub>3</sub> NWs, as shown in Figure 1c and d. The smaller particles are crystallized in tandem with phase conversion to β-AgVO<sub>3</sub> and we suggest that ionic diffusion to the surface facilitates a high density of small NPs observed and confirmed by electron microscopy, Raman scattering and X-ray diffraction. The lattice fringes of the Ag NPs have a spacing of ~0.2 nm, corresponding to the (200) plane for cubic silver.

XPS spectra for α-AgVO<sub>3</sub> and β-AgVO<sub>3</sub> NWs are presented in Figure 3. The O 1s and V 2p regions for as-synthesized α-AgVO<sub>3</sub> and heated β-AgVO<sub>3</sub> NWs are shown in Figure 3e,f. The photoemission at 517 eV and 524 eV corresponding to hyperfine splitting of the V 2p core level, and are observed from both material phases. Two peaks are present in the O 1s region for as-synthesized NWs. The peak at 530 eV may be attributed to O in AgO<sup>44</sup> and the peak at 532 eV corresponds to surface carbonisation of the presence of hydroxyls on the surface of the NWs most likely due to residual (C<sub>3</sub>H<sub>6</sub>O·C<sub>2</sub>H<sub>4</sub>O)<sub>x</sub> after hydrothermal treatment. Only a single core-level emission at 530 eV is seen in the XPS spectra for the β-AgVO<sub>3</sub> NWs after heating, implying that any surface residue has been removed via annealing. In the Ag 3d region of the XPS spectra in Figure 3g,h the two intense peaks at 368 and 374 eV are assigned to Ag 3d<sub>5/2</sub> and Ag 3d<sub>3/2</sub>, respectively, while the two stronger deconvoluted peaks at 368.4 and 374.4 eV can be assigned to Ag<sup>0</sup> 3d<sub>5/2</sub> and 3d<sub>3/2</sub>. In hydrothermally synthesized α-AgVO<sub>3</sub> NWs, we observe two characteristic weaker photoemission peaks at 367.4 and 373.4 eV corresponding to non-covalently bound, ionic Ag<sup>+</sup> 3d<sub>5/2</sub> and 3d<sub>3/2</sub> that exist as intercalated ions rather than Ag<sup>0</sup> within the AgVO<sub>3</sub>. After annealing, the Ag 3d<sub>5/2</sub> and Ag 3d<sub>3/2</sub> peaks consist of a single emission characteristic of Ag in its metallic state decorating the surface of the β-AgVO<sub>3</sub> NWs. This suggests that there is a higher content of metallic silver after annealing which is in close agreement with observations in TEM images and XRD analysis.

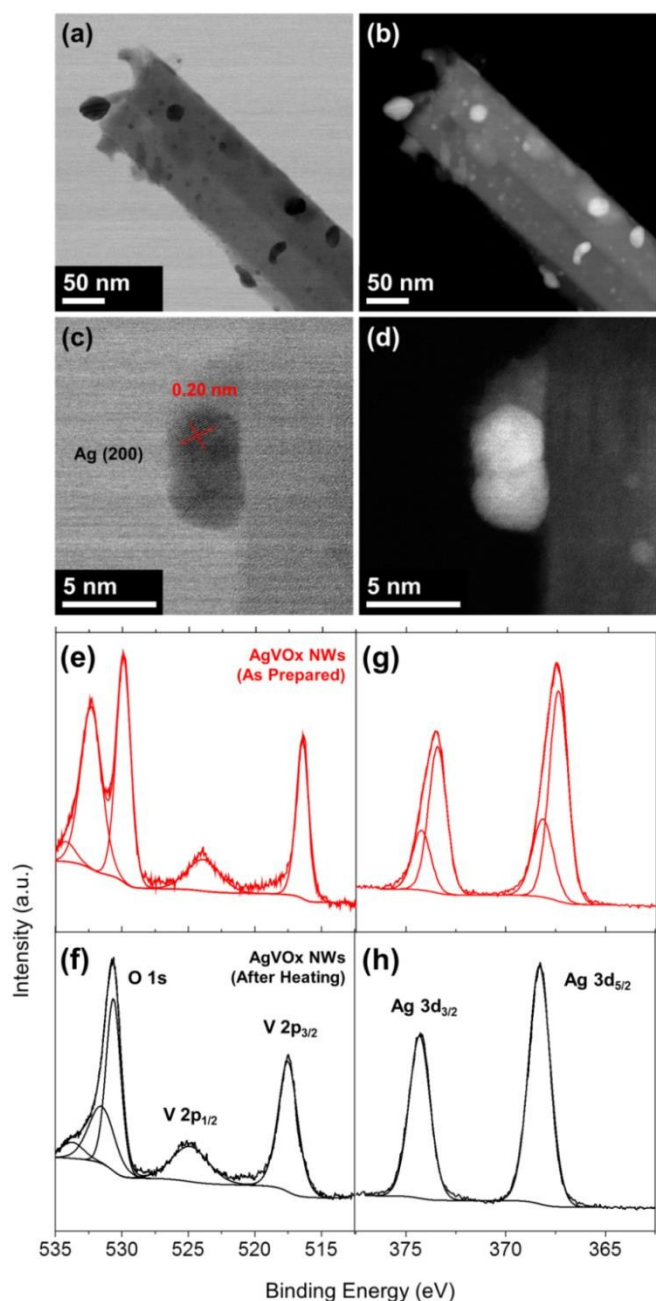


**Fig. 3.** Bright field (a) and dark field (b) STEM images of an Ag NP-decorated  $\beta$ -AgVO<sub>3</sub> NW. Bright field (c) and dark field (d) STEM images of an Ag NP. XPS spectra of O 1s and V 2p regions for AgVO<sub>x</sub> NWs (e) before and (f) after heating to 475 °C in N<sub>2</sub>, XPS spectra of the Ag 3d region for AgVO<sub>x</sub> NWs (g) before and (h) after heating to 475 °C in N<sub>2</sub>.

In order to investigate the oxidation state of the heated  $\beta$ -AgVO<sub>3</sub> NWs and the nature of the Ag NP-NW interface across their surface, electron energy loss (EELS) spectra were acquired over multiple areas of a typical heated NW, from the outer NP surface to the NW sub-surface region. A HAADF STEM image of a typical  $\beta$ -AgVO<sub>3</sub> NW is shown in Figure 4a. The interface between the NP and the NW body was specifically chosen so as to lie along the beam propagation direction, providing a clear projection of the structure and facilitating the study of any chemical bonding taking place between the metal and the oxide wire. EELS V L and Ag M edge maps corresponding to the area highlighted in Figure 4a are shown in Figure 4 b and c, respectively. A coloured overlay of both edge

maps, demonstrating the distribution of V and Ag in the  $\beta$ -AgVO<sub>3</sub> NWs is shown in Figure 4d. The EELS edge maps confirm that the NPs on the surface of the  $\beta$ -AgVO<sub>3</sub> NWs are pure Ag and do not contain any vanadium. Figure 4 d indicates that the  $\beta$ -AgVO<sub>3</sub> NWs may have a core-shell like electronic structure with the vanadium present in the outer shell having a different oxidation state than in the inner core. Also the chemical maps suggest that the outer shell contains less Ag (and more V) than in the core of the NW.

EELS spectra were extracted across areas 1 – 4 from Figure 4d to investigate the oxidation state of the NW surface and the interface between a NW and an Ag NP. The EELS spectra for each area are shown in Figure 4e. The EELS spectra for areas 1, 2 and 3 represent the outer surface of the  $\beta$ -AgVO<sub>3</sub> NW, with area 2 being close to the interface with an Ag NP, area 4 represents the surface of the core of the  $\beta$ -AgVO<sub>3</sub> NW. When traversing the  $\beta$ -AgVO<sub>3</sub> NW the electron beam can cause excitations from V 2p core states to unoccupied 3d states, losing the corresponding energy and resulting in two peaks in the collected loss spectra, L<sub>3</sub> (2p<sub>3/2</sub>→3d) and L<sub>2</sub> (2p<sub>1/2</sub>→3d), or so-called white lines, which are due to spin-orbit splitting.<sup>45</sup>

Vanadium L<sub>3</sub> and L<sub>2</sub> edges were observed in the EELS spectra for area 1 at 516.6 and 523.4 eV, which are similar to the V L<sub>3</sub> and L<sub>2</sub> edges for area 3 which were observed at 516.4 and 522.9 eV. This suggests that there is little variation in the vanadium oxidation state along the outer surface of the  $\beta$ -AgVO<sub>3</sub> NW for regions which do not contain Ag NPs. However, at the interface with an Ag NP (area 2) the V L<sub>3</sub> and L<sub>2</sub> edges are shifted to higher energies of 517.6 and 524.2 eV respectively, implying that vanadium on the outer surface of the NW is present in different oxidation states for regions with and without Ag NPs. The EELS spectrum for the core of the  $\beta$ -AgVO<sub>3</sub> NW (area 4) appears to be a convolution of the EELS spectra for area 2 and 3, i.e. a region of the outer surface with and without an Ag NP. The V L<sub>3</sub> edge consists of a high intensity peak at 518.1 eV and a weak shoulder at 516.4 eV. Likewise the L<sub>2</sub> edge consists of a high intensity peak at 524.9 eV and a weak shoulder at 522.8 eV. The presence of a weak shoulder followed by a high intensity peak for the V L<sub>3</sub> and L<sub>2</sub> edges is similar to previously reported EELS spectra for VO<sub>2</sub>, with vanadium present in a V<sup>4+</sup> oxidation state.<sup>46</sup> The energies of the high intensity peaks in the V L<sub>3</sub> and L<sub>2</sub> edges in the spectrum for area 4 are quite close to the values observed in the spectrum for area 2. This indicates that the vanadium oxidation state under the Ag NPs is similar to the bulk of the NW. A series of EELS spectra were acquired over multiple areas of the  $\beta$ -AgVO<sub>3</sub> NW shown in Figure 4a, as shown in Figure S2 and are discussed in the supplementary information. By using the calibration curves previously reported by Chen et al.<sup>47</sup> we estimated the changes in the oxidation state of vanadium across the four areas shown in Figure 4d. The oxidation states of vanadium in areas 1 and 3, i.e. along regions of the outer surface of a  $\beta$ -AgVO<sub>3</sub> NW which do not contain Ag NPs, were quite similar with values of  $\sim$ V<sup>1.4+</sup> and  $\sim$ V<sup>1.2+</sup> respectively. At the interface with an Ag NP (area 2) the vanadium oxidation state increased to  $\sim$ V<sup>2.7+</sup>, and increased further to  $\sim$ V<sup>3.5+</sup> on the surface of the core of the NW (area 4). This may suggest that  $\beta$ -AgVO<sub>3</sub> NWs have a core-shell like chemical structure with vanadium present in different oxidation states on the outer surface and the inner core and at the interface with Ag NPs.

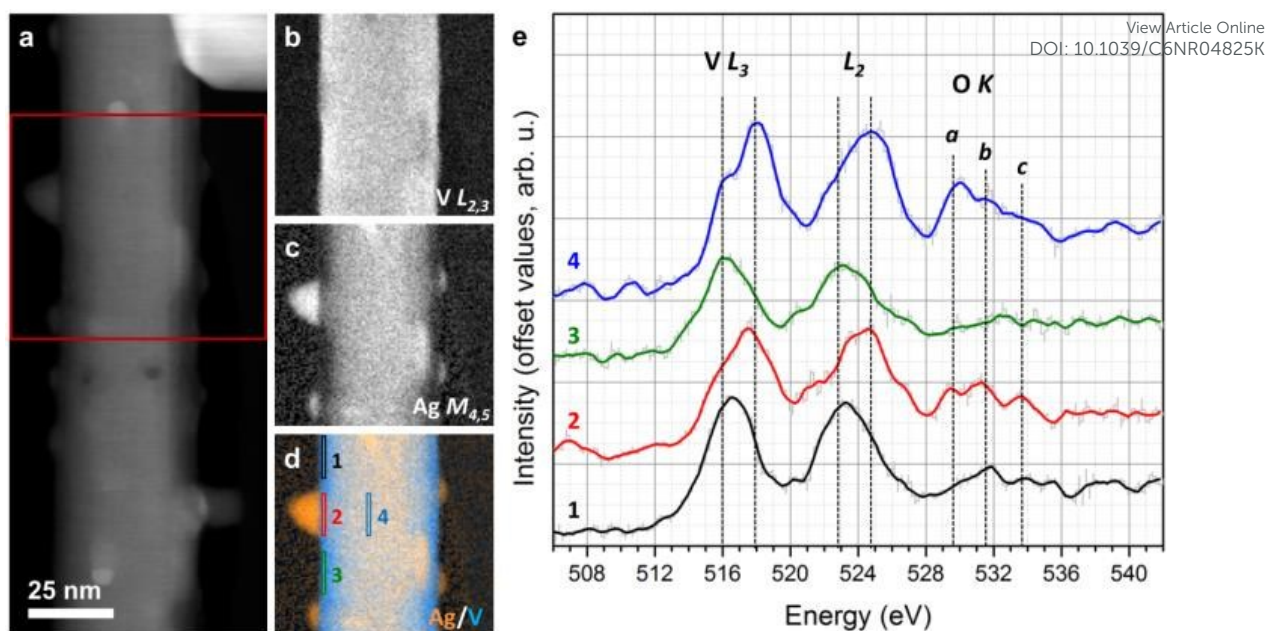


**Fig. 4.** (a) HAADF image of a typical  $\beta$ -AgVO<sub>3</sub> nanowire, EELS maps showing contributions from (b) V L and (c) Ag M edges, (d) an overlay of V L and Ag M edge maps demonstrating the distribution of V and Ag in the  $\beta$ -AgVO<sub>3</sub> NWs, (e) EELS spectra acquired from the four areas of the  $\beta$ -AgVO<sub>3</sub> NW highlighted in (d).

The variation in the vanadium oxidation state on the shell of the  $\beta$ -AgVO<sub>3</sub> NWs under an Ag NP and in regions without Ag NPs suggests that there is a good contact between the Ag NPs and the NWs. If the Ag NPs were not chemically bound to the NWs we would not expect any variation in the oxidation state. By comparison, TiO<sub>2</sub> nanotubes decorated with Ag NPs have been reported to demonstrate significantly improved electrochemical performance over non-decorated nanotubes.<sup>48</sup> The enhanced performance was attributed to improved electronic conductivity, obtained by providing highly conductive paths for electrons flowing through well-distributed Ag NPs deposited on the walls of the nanotubes. Chemically bound Ag NPs which are consequently in good electrical contact with the  $\beta$ -AgVO<sub>3</sub> NWs will likely increase the conductivity of the NWs and may remove the necessity to add a conductive additive and a binder. Also, Takeuchi et al. have reported that, during discharging, the Ag<sup>+</sup> in Ag<sub>2</sub>VO<sub>2</sub>PO<sub>4</sub> is reduced *in-situ* to metallic silver, forming a conductive silver metal matrix within the SVPO cathode, thereby enhancing the electrical conductivity of the material.<sup>49</sup> EELS mapping of the Ag M edge of the  $\beta$ -AgVO<sub>3</sub> NWs indicates the Ag is present within the NWs core of the NWs containing more than the outer shell. A reduction of Ag<sup>+</sup> in the core of the  $\beta$ -AgVO<sub>3</sub> NWs during discharge to metallic Ag may further improve the conductivity of the NWs. The effects of discharging the  $\beta$ -AgVO<sub>3</sub> NWs on their structure will be discussed after the electrochemical characterization of the NWs.

Previous reports have suggested that the electrochemical performance of  $\beta$ -AgVO<sub>3</sub> is superior to  $\alpha$ -AgVO<sub>3</sub>, where the tunnel structure enhances cation insertion. In order to investigate this proposal and to determine the effectiveness of conductive Ag NP decoration of the NW networked cathode material, the electrochemical performance of  $\alpha$ -AgVO<sub>3</sub> and  $\beta$ -AgVO<sub>3</sub> NWs were systematically compared via cyclic voltammetry and galvanostatic testing. Cyclic voltammetry curves for  $\alpha$ -AgVO<sub>3</sub> and  $\beta$ -AgVO<sub>3</sub> NWs are shown in Figure 5a and b, respectively. A weak cathodic peak

was observed in the first scan for the  $\alpha$ -AgVO<sub>3</sub> NWs at 2.85 V, corresponding to the reduction of Ag<sup>+</sup> → Ag<sup>0</sup>. In situ energy dispersive x-ray diffraction measurements of Li/Ag<sub>2</sub>VP<sub>2</sub>O<sub>8</sub> have previously demonstrated that during discharge, Ag metal is formed at the electrode-electrolyte interface; here we also demonstrate evidence of Ag metal forming in the initial cathodic scan.<sup>50, 51</sup> A strong cathodic peak was observed at 2.35 V, corresponding to the reduction of V<sup>5+</sup> → V<sup>4+</sup>. The profile of the first scan for the as-prepared NWs is in close agreement with previously reported results for  $\alpha$ -AgVO<sub>3</sub>.<sup>52</sup> The strong cathodic peak in the first cycle is not present in subsequent cycles indicating that for  $\alpha$ -AgVO<sub>3</sub>, the reduction of V<sup>5+</sup> → V<sup>4+</sup> is not a reversible process.

Three strong cathodic peaks were observed in the first scan for  $\beta$ -AgVO<sub>3</sub> NWs at 2.85, 2.28 and 1.98 V, as shown in Figure 5b. It has previously been reported that peaks observed in the range of 3.2 – 2.75 V are due to the reduction of V<sup>5+</sup> and Ag<sup>+</sup>.<sup>12, 53</sup> The broad peak centred at 2.85 V contains a weak shoulder at 2.74 V which is likely due to an overlap of V<sup>5+</sup> and Ag<sup>+</sup> reduction peaks. This is consistent with the simultaneous formation of V<sup>4+</sup> and Ag<sup>0</sup>, which has previously been shown to occur in this potential range. The Ag reduction peak at 2.85 V for  $\beta$ -AgVO<sub>3</sub> NWs is far more significant than the weak peak observed at 2.85 V for  $\alpha$ -AgVO<sub>3</sub> NWs, which again suggests that there is a greater metallic silver content for the  $\beta$ -AgVO<sub>3</sub> NWs after annealing from the Ag<sup>+</sup> containing  $\alpha$ -AgVO<sub>3</sub> NW structures. The remaining cathodic peaks at 2.28 and 1.98 V can be assigned to V<sup>5+</sup> → V<sup>4+</sup> and V<sup>4+</sup> → V<sup>3+</sup> reductions, respectively. The anodic peaks at 2.70 and 3.08 V resulted from the oxidation of V<sup>3+</sup> → V<sup>4+</sup> and the partial oxidation of V<sup>4+</sup> → V<sup>5+</sup>, respectively. After the first scan the broad peak centred at 2.85 V is no longer present, indicating that an irreversible reaction has occurred during the first cycle; i.e. the reduction of Ag<sup>+</sup> → Ag<sup>0</sup>, may not be a reversible reaction and the initial electrochemical reactions ensure remaining ionic silver close to the  $\beta$ -AgVO<sub>3</sub> NW surface is reduced to metallic silver, improving the likelihood for inter-wire contacting. The two

vanadium reduction peaks at 2.28 and 1.98 V can be seen in the second cycle; these distinct peaks became smooth curves in the 5<sup>th</sup> and 10<sup>th</sup> scans.

$\alpha$ -AgVO<sub>3</sub> and  $\beta$ -AgVO<sub>3</sub> NWs were cycled as lithium battery cells galvanostatically using specific currents ranging from 25 – 100 mA/g. The voltage profiles for  $\alpha$ -AgVO<sub>3</sub> NWs for the first cycle using specific currents of 25, 50 and 100 mA/g are shown in Figure 5c. A weak plateau can be seen in the first discharge curve at a specific current of 25 mA/g at 2.85 V, corresponding to the initial reduction of Ag<sup>+</sup> → Ag<sup>0</sup> and the weak cathodic peak observed at the same potential during the first CV scan as shown in Figure 5a. A wide plateau can be seen in the first discharge curve from 2.5 – 2.3 V, which again is in excellent agreement with the strong cathodic peak observed in the first CV scan for  $\alpha$ -AgVO<sub>3</sub> NWs. The discharge and charge profiles for  $\beta$ -AgVO<sub>3</sub> NWs cycled at specific currents of 25, 50 and 100 mA/g are shown in Figure 5d. The voltage profile for the first discharge contains 3 sloping potential ranges which correspond to the three cathodic peaks in the CV scan in Figure 5b. The first plateau from 3.04 – 2.42 V is associated with the reduction of Ag<sup>+</sup> → Ag<sup>0</sup>, the second and third plateaux from 2.39 – 2.12 V and 2.10 – 1.6 V are due to the reduction of V<sup>5+</sup> → V<sup>4+</sup> and V<sup>4+</sup> → V<sup>3+</sup>, respectively.<sup>54, 55</sup> The presence of three distinct voltage plateaux in the first discharge curve is in close agreement with previous reports on the electrochemical performance of other  $\beta$ -AgVO<sub>3</sub> nanostructures.<sup>4, 56</sup>

The specific capacity values obtained for the first 20 cycles for  $\alpha$ -AgVO<sub>3</sub> and  $\beta$ -AgVO<sub>3</sub> NWs at specific currents of 25, 50 and 100 mA/g are shown in Figure 5e. Both  $\alpha$ -AgVO<sub>3</sub> and  $\beta$ -AgVO<sub>3</sub> NWs suffer from a significant initial capacity fade; however, from the second cycle onwards the capacity retention is far more stable. The specific capacity obtained for  $\alpha$ -AgVO<sub>3</sub> NWs at a specific current of 25 mA/g after the 1<sup>st</sup> discharge was 190 mAh/g. After the 10<sup>th</sup> discharge the capacity decreased to 28 mAh/g. The capacity retention of the  $\alpha$ -AgVO<sub>3</sub> NWs increased after the 10<sup>th</sup> cycle with the capacity decreasing slightly to 26 mAh/g after the 20<sup>th</sup> discharge. The capacity values obtained for  $\alpha$ -AgVO<sub>3</sub> NWs decreased slightly with increased specific current. The highest capacities for the  $\beta$ -AgVO<sub>3</sub> NWs were obtained at the lowest specific current. The initial discharge capacity for  $\beta$ -AgVO<sub>3</sub> NWs at a specific current of 25 mA/g was 175 mAh/g, this value decreased to ~50 mAh/g after the 10<sup>th</sup> discharge and decreased slightly further to 43 mAh/g after the 20<sup>th</sup> discharge. These capacities are comparable to <sup>4</sup> or greater than <sup>3, 13, 54, 57</sup> previously reported values for various SVO nanostructures. From Figure 5e it is clear that significantly higher specific capacity values were obtained from the  $\beta$ -AgVO<sub>3</sub> NWs; this supports previously reported theories that the electrochemical performance of  $\beta$ -AgVO<sub>3</sub> is superior to  $\alpha$ -AgVO<sub>3</sub>. Here, we show that diffusional outflux of Ag ions from the  $\alpha$ -AgVO<sub>3</sub> phase during recrystallization to the  $\beta$ -AgVO<sub>3</sub> affects the electronic nature of the vanadate and its surface coating with covalently bound Ag NPs, thereby improving the electrochemical response<sup>13</sup>

To investigate the structural effects of lithium insertion and removal on  $\beta$ -AgVO<sub>3</sub> NWs TEM images after the first galvanostatic discharge and charge were acquired and are shown in Figure 6a and b, respectively. Initially  $\beta$ -AgVO<sub>3</sub> NWs were decorated with many small Ag NPs (~5 nm), after the first discharge the Ag NPs are much

larger (~30–40 nm) as shown in Figure 6a. As discussed earlier, it has been proposed that during discharge, Ag<sup>+</sup> present between the van der Waals layers of vanadium oxide octahedra is reduced to Ag<sup>0</sup> and redeposited, allowing Li<sup>+</sup> to then occupy the available sites in the vanadate structure and alloy with the Ag metal.<sup>11</sup> The larger NPs shown in Figure 6 are consistently found after discharge and subsequent recharge and thus may be due to Ag<sup>+</sup> being reduced to metallic silver and depositing near the sites on the NWs that already contained Ag NPs formed by thermal conversion to Ag NP-decorated  $\beta$ -AgVO<sub>3</sub>. After the first charge (Figure 6b) the Ag NPs remain approximately the same size, indicating that the initial reduction of Ag<sup>+</sup> is a non-reversible reaction, which is in close agreement with observations in cyclic voltammetry and may explain the significant capacity fade after the first cycle, where this process occurs. The NWs after the first charge are generating significantly less electron scattering in otherwise identical observation conditions than after the first discharge, as shown in Figure 6b. This is most likely due to the removal of Li<sup>+</sup> during charging, the resulting core structure becoming far less dense.

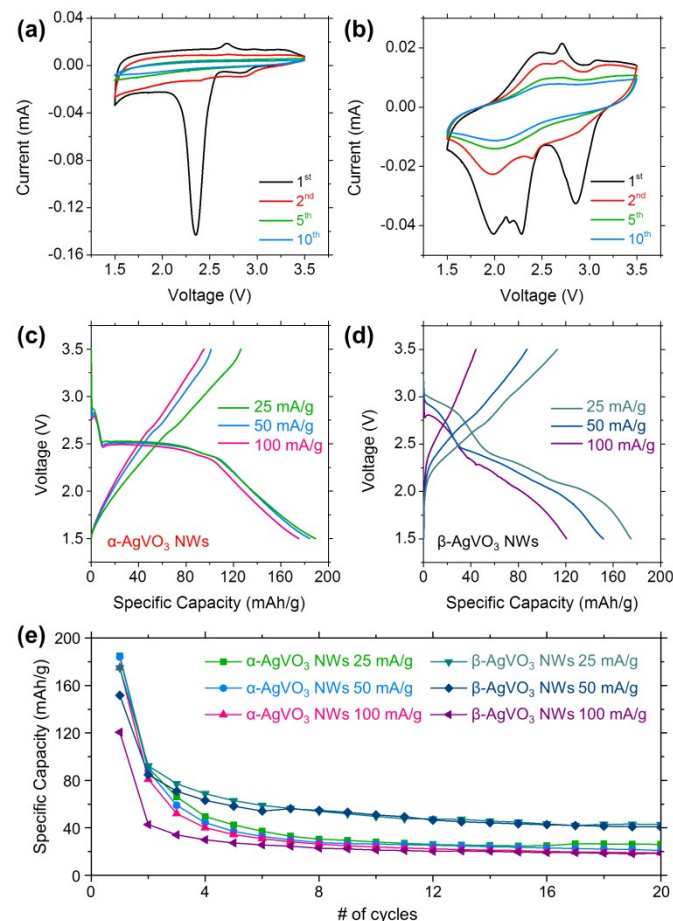


**Fig. 5.** Cyclic voltammograms for (a)  $\alpha$ -AgVO<sub>3</sub> and (b)  $\beta$ -AgVO<sub>3</sub> NWs, acquired at a scan rate of 0.1 mV s<sup>-1</sup>. Discharge and charge voltage profiles for the first cycle for (c)  $\alpha$ -AgVO<sub>3</sub> and (d)  $\beta$ -AgVO<sub>3</sub> NWs at a specific currents of 25, 50 and 100 mA/g. (e) Comparison of specific capacity values for  $\alpha$ -AgVO<sub>3</sub> and  $\beta$ -AgVO<sub>3</sub> NWs at a specific currents of 25, 50 and 100 mA/g.

The XPS spectra for heated AgVO<sub>x</sub> NWs after the first discharge and after the first charge are shown in Figure 6c-f. The peak observed at ~ 530 eV in the O 1s region for both samples may be attributed to O in AgO.<sup>44</sup> The peak observed at 532 eV, which was

not present after heating to 475 °C (Figure 3f), is present again after the first discharge and the first charge. This peak is related to a C=O bond and is likely due to the presence of residual electrolyte after electrochemical testing. Two additional peaks were observed after the first charge which were not present after the initial discharge. These peaks at ~ 528.6 and ~ 533.1 eV may be assigned to O in Ag<sub>2</sub>O and adsorbed water respectively.<sup>44</sup> The indication of the presence of Ag<sub>2</sub>O suggests that, after the first charge, there is a partial oxidation of Ag to Ag<sub>2</sub>O. This implies that the formation of Ag during the first discharge is not a completely irreversible process.

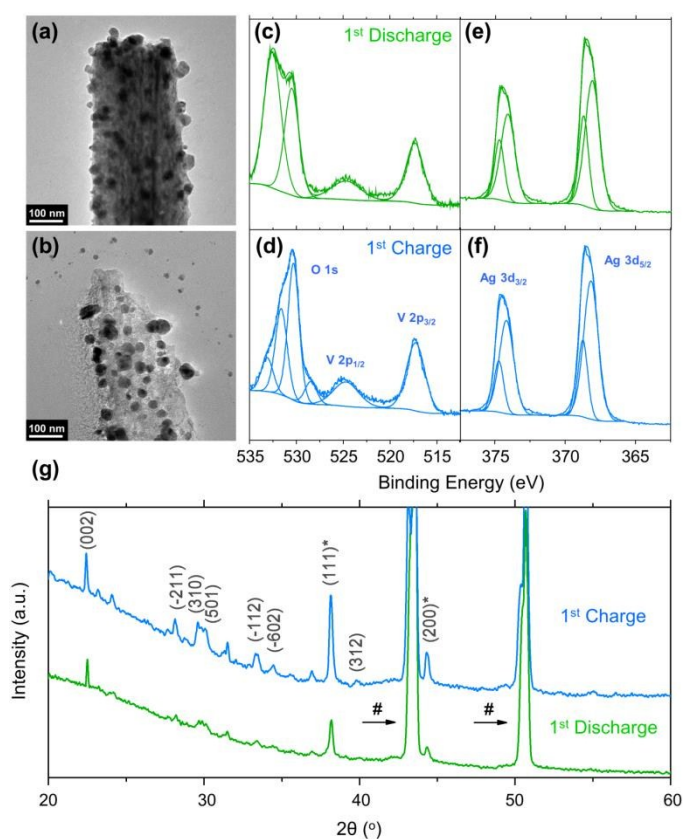


**Fig. 6.** TEM images of  $\beta$ -AgVO<sub>3</sub> NWs (a) after the 1<sup>st</sup> discharge and (b) after the 1<sup>st</sup> charge. XPS spectra of O 1s and V 2p regions for  $\beta$ -AgVO<sub>3</sub> NWs (c) after the first discharge and (d) after the first charge. XPS spectra of the Ag 3d region for  $\beta$ -AgVO<sub>3</sub> NWs (e) after the first discharge and (f) after the first charge. (g) XRD patterns of  $\beta$ -AgVO<sub>3</sub> NWs after the 1<sup>st</sup> discharge and 1<sup>st</sup> charge. The reflections labelled # are from the stainless steel current collector. Reflections labelled with \* correspond to cubic Ag.

While the binding energy for the V 2p<sub>3/2</sub> peak does not vary after the first discharge and the first charge, the full-width at half-maximum (FWHM) varies significantly from 1.712 eV, initially after heating, to 2.214 eV after the first discharge and 2.297 eV after the first charge. The FWHM does not return to its initial value, indicating that an irreversible reaction has occurred during the first cycle that has changed the entire core-level electronic environment. After the first discharge and charge the Ag 3d<sub>5/2</sub> and Ag 3d<sub>3/2</sub> core-level emission can be deconvoluted to consist of two photoemission peaks, similar to the as-synthesized AgVO<sub>x</sub> NWs. There is an increase in the amounts of Ag<sup>+</sup> 3d<sub>5/2</sub> and 3d<sub>3/2</sub> present in the two weaker deconvoluted peaks at 367.4 and 373.4 eV compared to the as-prepared material. The relative intensity of these peaks

decreases after the first charge. The presence of peaks associated with Ag<sup>0</sup> and Ag<sup>+</sup> in the XPS spectrum for  $\beta$ -AgVO<sub>3</sub> NWs suggests that Li<sup>+</sup> have interacted with the Ag NPs present on the surface and the Ag present in the silver vanadium oxide crystal structure. After the first charge the relative intensity of the Ag<sup>0</sup> 3d<sub>5/2</sub> and 3d<sub>3/2</sub> and the Ag<sup>+</sup> 3d<sub>5/2</sub> and 3d<sub>3/2</sub> core-level emission intensity is reduced, but not quenched entirely, which again is indicative of an irreversible reaction occurring during the first discharge.

The XRD patterns for  $\beta$ -AgVO<sub>3</sub> NWs after the first discharge and charge are shown in Figure 6g. Both samples can be indexed to  $\beta$ -AgVO<sub>3</sub> phase, a *Cm* space group (JCPDS 00-029-1154). After the first discharge the highest intensity peak, other than the reflections for cubic Ag, is the (002) reflection for  $\beta$ -AgVO<sub>3</sub>. The relative intensity for this peak is much higher than in the XRD pattern for the  $\beta$ -AgVO<sub>3</sub> NWs shown in Figure 2c. This suggests that Li<sup>+</sup> may be intercalated in this plane of the  $\beta$ -AgVO<sub>3</sub> crystal structure. After the first discharge the relative intensities for all other reflections are lower than prior to electrochemical testing; however after the first charge and the removal of Li<sup>+</sup> the intensities increase. XPS analysis indicates that Ag is oxidised to form Ag<sub>2</sub>O during the first charge. This implies that the initial reduction of Ag<sup>+</sup> to cubic Ag during the first discharge is reversible to some degree. Consequently, there is an increase in the relative intensities of  $\beta$ -AgVO<sub>3</sub> reflections after the first charge.

## Conclusions

$\alpha$ -AgVO<sub>3</sub> NWs decorated with Ag NPs were successfully prepared by a hydrothermal treatment of a mixture of ammonium metavanadate and silver nitrate. Heating the as-prepared NWs to 475 °C in N<sub>2</sub> results in a structural conversion from  $\alpha$ -AgVO<sub>3</sub> to  $\beta$ -AgVO<sub>3</sub>. Thermogravimetric analysis was performed to monitor the transition, and revealed that only ~7% of the initial mass of the  $\alpha$ -AgVO<sub>3</sub> NWs was lost during heating. X-ray diffraction, electron diffraction and Raman spectroscopy all confirm that the heated NWs are indeed  $\beta$ -AgVO<sub>3</sub> NWs decorated with Ag NPs. XPS of the NWs before and after heating indicates that the as-prepared  $\alpha$ -AgVO<sub>3</sub> NWs contain Ag in multiple oxidation states whereas Ag is predominately present in just one oxidation state in the heated  $\beta$ -AgVO<sub>3</sub> NWs. During phase conversion to the tunnel structured  $\beta$ -AgVO<sub>3</sub> phase, migration of ionic Ag to the outer surface results in a high density of NPs in reduced, metallic form that provide electrical bridging between NWs. EELS spectroscopy indicates that the oxidation state of vanadium varies across the surface of a  $\beta$ -AgVO<sub>3</sub> NW, suggesting that  $\beta$ -AgVO<sub>3</sub> NWs may have a core-shell like compositional structure. Cyclic voltammetry of the  $\alpha$ -AgVO<sub>3</sub> and  $\beta$ -AgVO<sub>3</sub> NWs decorated with Ag NPs suggests that the reduction of Ag<sup>+</sup> → Ag<sup>0</sup> occurs prior to the reduction of vanadium. From comparing the first cycle for both materials at a scan rate of 0.1 mV/s it is clear that there is a significant difference in the electrochemical response of  $\alpha$ -AgVO<sub>3</sub> and  $\beta$ -AgVO<sub>3</sub>. One strong cathodic peak was observed in the first cycle for the  $\alpha$ -AgVO<sub>3</sub> NWs whereas three strong cathodic peaks were observed for  $\beta$ -AgVO<sub>3</sub>. The capacity values obtained for  $\beta$ -AgVO<sub>3</sub> NWs are significantly higher than those obtained for the  $\alpha$ -AgVO<sub>3</sub> NWs, confirming that the electrochemical performance of  $\beta$ -AgVO<sub>3</sub> is superior to  $\alpha$ -

AgVO<sub>3</sub>. Structural characterisation of β-AgVO<sub>3</sub> NWs gives insight into the Li<sup>+</sup> reaction mechanism for β-AgVO<sub>3</sub>. TEM and XPS analysis confirm that Ag<sup>+</sup> within the β-AgVO<sub>3</sub> structure is reduced to metallic Ag during discharge.

## Acknowledgements

This work was also supported by Science Foundation Ireland (SFI) through an SFI Technology Innovation and Development Award under contract no. 13/TIDA/E2761. This publication has also emanated from research supported in part by a research grant from SFI under Grant Number 14/IA/2581.

## Notes and references

1. K. J. Takeuchi, A. C. Marschilok, S. M. Davis, R. A. Leising and E. S. Takeuchi, *Coord. Chem. Rev.*, 2001, **219–221**, 283-310.
2. A. M. Crespi, S. K. Somdahl, C. L. Schmidt and P. M. Skarstad, *J. Power Sources*, 2001, **96**, 33-38.
3. Z. Chen, S. Gao, R. Li, M. Wei, K. Wei and H. Zhou, *Electrochim. Acta*, 2008, **53**, 8134-8137.
4. S. Liang, J. Zhou, A. Pan, X. Zhang, Y. Tang, X. Tan, T. Chen and R. Wu, *J. Power Sources*, 2013, **228**, 178-184.
5. E. S. Takeuchi, A. C. Marschilok, K. Tanzil, E. S. Kozarsky, S. Zhu and K. J. Takeuchi, *Chem. Mater.*, 2009, **21**, 4934-4939.
6. X. Tian, X. Xu, L. He, Q. Wei, M. Yan, L. Xu, Y. Zhao, C. Yang and L. Mai, *J. Power Sources*, 2014, **255**, 235-241.
7. E. S. Takeuchi and W. C. Thiebolt, *J. Electrochem. Soc.*, 1988, **135**, 2691-2694.
8. R. A. Leising, W. C. Thiebolt and E. S. Takeuchi, *Inorg. Chem.*, 1994, **33**, 5733-5740.
9. R. A. Leising and E. S. Takeuchi, *Chem. Mater.*, 1994, **6**, 489-495.
10. R. A. Leising and E. S. Takeuchi, *Chem. Mater.*, 1993, **5**, 738-742.
11. S. Zhang, W. Li, C. Li and J. Chen, *J. Phys. Chem. B*, 2006, **110**, 24855-24863.
12. E. S. Takeuchi and P. Piliero, *J. Power Sources*, 1987, **21**, 133-141.
13. H. Zeng, Q. Wang and Y. Rao, *RSC Adv.*, 2015, **5**, 3011-3015.
14. Y. Wu, P. Zhu, X. Zhao, M. V. Reddy, S. Peng, B. V. R. Chowdari and S. Ramakrishna, *J. Mater. Chem. A*, 2013, **1**, 852-859.
15. C. Han, Y. Pi, Q. An, L. Mai, J. Xie, X. Xu, L. Xu, Y. Zhao, C. Niu, A. M. Khan and X. He, *Nano Lett.*, 2012, **12**, 4668-4673.
16. C. Xiong, A. E. Aliev, B. Gnade and K. J. Balkus, *ACS Nano*, 2008, **2**, 293-301.
17. M. C. Artal, R. D. Holtz, F. Kummrow, O. L. Alves and G. d. A. Umbuzeiro, *Environ. Toxicol. Chem.*, 2013, **32**, 908-912.
18. J. Li, L.-F. Zheng, K.-F. Zhang, X.-Q. Feng, Z.-X. Su and J.-T. Ma, *Mater. Res. Bull.*, 2008, **43**, 2810-2817.
19. L. Mai, L. Xu, Q. Gao, C. Han, B. Hu and Y. Pi, *Nano Lett.*, 2010, **10**, 2604-2608.
20. A. Singh, D. P. Dutta, A. Ballal, A. K. Tyagi and M. H. Fulekar, *Mater. Res. Bull.*, 2014, **51**, 447-454.
21. Z. Wei, L. Feng, J. Zhi-Ming, S. Xiao-Bo, Y. Peng-Hui, W. Xue-Ren, S. Cheng, G. Zhan-Qi and L. Jiang-Sheng, *J. Mater. Chem. A*, 2014, **2**, 13226-13231.
22. Q. Deng, X. Duan, D. H. L. Ng, H. Tang, Y. Yang, M. Kong, Z. Wu, W. Cai and G. Wang, *ACS Appl. Mater. Interfaces*, 2012, **4**, 6030-6037.
23. K.-H. Chen, Y.-C. Pu, K.-D. Chang, Y.-F. Liang, C.-M. Liu, J.-W. Yeh, H.-C. Shih and Y.-J. Hsu, *J. Phys. Chem. C*, 2012, **116**, 19039-19045.
24. S. Liu, J. Tian, L. Wang and X. Sun, *Carbon*, 2011, **49**, 3158-3164.
25. J. He, W. Wang, Z. Zou, F. Long and Z. Fu, *Ionics*, 2014, **20**, 1063-1070.
26. C. Venkateswara Rao, A. Leela Mohana Reddy, Y. Ishikawa and P. M. Ajayan, *ACS Appl. Mater. Interfaces*, 2011, **3**, 2966-2972.
27. L. Fransson, T. Eriksson, K. Edström, T. Gustafsson and J. O. Thomas, *J. Power Sources*, 2001, **101**, 1-9.
28. R. Dominko, M. Gaberscek, J. Drogenik, M. Bele, S. Pejovnik and J. Jamnik, *J. Power Sources*, 2003, **119–121**, 770-773.
29. X.-Y. Liu, H.-J. Peng, Q. Zhang, J.-Q. Huang, X.-F. Liu, L. Wang, X. He, W. Zhu and F. Wei, *ACS Sustain. Chem. Eng.*, 2014, **2**, 200-206.
30. Y. Wu, Y. Wei, J. Wang, K. Jiang and S. Fan, *Nano Lett.*, 2013, **13**, 818-823.
31. B. Guo, X. Wang, P. F. Fulvio, M. Chi, S. M. Mahurin, X.-G. Sun and S. Dai, *Adv. Mater.*, 2011, **23**, 4661-4666.
32. B.-L. He, B. Dong and H.-L. Li, *Electrochem. Commun.*, 2007, **9**, 425-430.
33. S. Huang, Z. Wen, J. Zhang, Z. Gu and X. Xu, *Solid State Ion.*, 2006, **177**, 851-855.
34. S.-J. Bao, Q.-L. Bao, C.-M. Li, T. P. Chen, C.-Q. Sun, Z.-L. Dong, Y. Gan and J. Zhang, *Small*, 2007, **3**, 1174-1177.
35. G. Li, K. Chao, C. Ye and H. Peng, *Mater. Lett.*, 2008, **62**, 735-738.
36. J.-M. Song, Y.-Z. Lin, H.-B. Yao, F.-J. Fan, X.-G. Li and S.-H. Yu, *ACS Nano*, 2009, **3**, 653-660.
37. S. Liang, J. Zhou, A. Pan, Y. Li, T. Chen, Z. Tian and H. Ding, *Mater. Lett.*, 2012, **74**, 176-179.
38. Q. Bao, S. Bao, C. M. Li, X. Qi, C. Pan, J. Zang, W. Wang and D. Y. Tang, *Chem. Mater.*, 2007, **19**, 5965-5972.
39. H. Tian, I. E. Wachs and L. E. Briand, *J. Phys. Chem. B*, 2005, **109**, 23491-23499.
40. R. Lewandowska, K. Krasowski, R. Bacewicz and J. E. Garbarczyk, *Solid State Ion.*, 1999, **119**, 229-234.
41. V. Sivakumar, R. Suresh, K. Giribabu and V. Narayanan, *Solid State Sci.*, 2015, **39**, 34-39.
42. J. Yu and A. Kudo, *Adv. Funct. Mater.*, 2006, **16**, 2163-2169.
43. S. Kittaka, K. Matsuno and H. Akashi, *J. Solid State Chem.*, 1999, **142**, 360-367.
44. B. V. Crist, *Wiley-VCH*, 2000, **1**, 37-40.
45. X. Liu, C. Täschner, A. Leonhardt, M. H. Rummeli, T. Pichler, T. Gemming, B. Büchner and M. Knupfer, *Phys. Rev. B*, 2005, **72**, 115407.
46. M. Chi, T. Mizoguchi, L. W. Martin, J. P. Bradley, H. Ikeno, R. Ramesh, I. Tanaka and N. Browning, *J. Appl. Phys.*, 2011, **110**, 046104.
47. J. G. Chen, C. M. Kirn, B. Frühberger, B. D. DeVries and M. S. Touvelle, *Surf. Sci.*, 1994, **321**, 145-155.

## ARTICLE

## Journal Name

48. S. A. Pervez, U. Farooq, A. Yaqub, C.-H. Doh, D. Kim, S. Sim, M. Hwang, J.-H. Choi and Y.-J. Lee, *J. Korean Phys. Soc.*, 2013, **63**, 1809-1814.
49. A. C. Marschilok, E. S. Kozarsky, K. Tanzil, S. Zhu, K. J. Takeuchi and E. S. Takeuchi, *J. Power Sources*, 2010, **195**, 6839-6846.
50. E. S. Takeuchi, A. C. Marschilok, K. J. Takeuchi, A. Ignatov, Z. Zhong and M. Croft, *Energy Environ. Sci.*, 2013, **6**, 1465-1470.
51. K. Kirshenbaum, D. C. Bock, C.-Y. Lee, Z. Zhong, K. J. Takeuchi, A. C. Marschilok and E. S. Takeuchi, *Science*, 2015, **347**, 149-154.
52. F. Cheng and J. Chen, *J. Mater. Chem.*, 2011, **21**, 9841-9848.
53. L. Mai, X. Xu, C. Han, Y. Luo, L. Xu, Y. A. Wu and Y. Zhao, *Nano Lett.*, 2011, **11**, 4992-4996.
54. R. P. Ramasamy, C. Feger, T. Strange and B. N. Popov, *J. Appl. Electrochem.*, 2006, **36**, 487-497.
55. L. Liang, Y. Xu, Y. Lei and H. Liu, *Nanoscale*, 2014, **6**, 3536-3539.
56. S. Liang, J. Zhou, X. Zhang, Y. Tang, G. Fang, T. Chen and X. Tan, *CrystEngComm*, 2013, **15**, 9869-9873.
57. K. West and A. M. Crespi, *J. Power Sources*, 1995, **54**, 334-337.

View Article Online  
DOI: 10.1039/C6NR04825K

Nanoscale Accepted Manuscript